Tunable resistive switching in 2D MXene Ti$_3$C$_2$ nanosheets for non-volatile memory and neuromorphic computing

Xuelian Zhang[1], Haohan Chen[1], Siqi Cheng[1], Feng Guo[2], Wenjing Jie[1]* and Jianhua Hao[2]*

[1] College of Chemistry and Materials Science, Sichuan Normal University, Chengdu, 610066, China

[2] Department of Applied Physics, The Hong Kong Polytechnic University, Hung Hom, Kowloon, Hong Kong, China.

KEYWORDS: memristor; 2D nanosheets; MXene; artificial synapse; neuromorphic computing

ABSTRACT

Artificial synapse is essential for neuromorphic computing which has been expected to overcome the bottleneck of traditional von-Neumann system. Memristors can work as an artificial synapse owing to its tunable non-volatile resistance states which offer the capabilities of information storage, processing and computing. In this work, memristors based on two-dimensional (2D) MXene Ti$_3$C$_2$ nanosheets sandwiched by Pt electrodes are investigated in terms of resistive switching (RS) characteristics, synaptic functions and neuromorphic computing. Digital and analog RS behaviors are found to coexist depending on the magnitude of operation voltage. Digital RS behaviors with two resistance states possessing a large switching ratio exceeding 10^3 can be achieved under a high operation voltage. Analog RS behaviors with a series of resistance states

exhibiting a gradual change can be observed at a relatively low operation voltage. Furthermore, artificial synapses can be implemented based on the memristors with the basic synaptic functions, such as long-term plasticity of long-term potentiation (LTP) and depression (LTD) as well as short-term plasticity of the paired-pulse facilitation (PPF) and depression (PPD). Moreover, the "learning-forgetting" experience is successfully emulated based on the artificial synapses. And more importantly, the artificial synapses can construct an artificial neural network to implement image recognition. The coexistence of digital and analog RS behaviors in the 2D Ti_3C_2 nanosheets suggest the potential applications in non-volatile memory and neuromorphic computing, which is expected to facilitate simplifying the manufacture complexity for complex neutral system where analog and digital switching are essential for information storage and processing.

INTRODUCTION

Neuromorphic computing, also termed as brain-like computing, is a method modeled after the human brain and neural system for computer engineering.[1] Neuromorphic computing has emerged as a promising candidate to overcome the limitations of the traditional von-Neumann computer in which the memory and processor are separated each other. Neuromorphic computing is aimed to solve the bottleneck of von-Neumann system through in-parallel storage and process of information with high-speed and low-power consumption.[2] Artificial neural network (ANN) attempts to work in analogy to the biological neural networks in which the basic units are the neurons with the biological synapse connecting them.[3,4] Therefore, the exploitation of artificial synapse that can mimic biological synapse has been becoming a hot topic nowadays. A memristor consists of two electrodes and a resistive switching (RS) layer between them, where the resistance can be reconfigured by electrical stimuli.[5,6] The memristors can be used to implement information storage as well as artificial synapse for the applications in neuromorphic computing owing to its voltage tunable RS properties which are essential to biological synapses.[7] In recent years, two-dimensional (2D) materials have been widely used as the RS layer in memristors due to their controllable ultra-thin thickness and unique electronic properties,[8] such as transition metal dichalcogenides (TMDs)[9] and boron nitride (BN).[10] In addition, memristors based on 2D materials can truly achieve nanoscale dimension and even a single atomic layer, contributing to low-power consumption, gate tunability and mechanical flexibility.[11,12] Furthermore, such memristors based on 2D materials are applicable to the artificial synapses for brain-

inspired neuromorphic computing.[13,14] The Ti_3C_2 as a well-studied 2D material in the

MXene family, has been widely used in supercapacitors,[15] batteries,[16] catalysts[17,18] and

biosensors.[19] In recent years, researches of Ti_3C_2 in memristors and memristor-based

artificial synapse has gradually emerged owing to its outstanding electric properties and

diverse structures,[20,21] but the research is still limited compared to other classes of

nanomaterials. Analog RS behaviors and basic synaptic functions were reported in

$Cu/Ti_3C_2/Cu$ memristors.[22] Moreover, digital RS behaviors and a 4-bit in memory

digital comparator were achieved based on oxidized Ti_3C_2 films with electrostatically

adsorbed Ag ions on the surface.[23] The digital RS is generally considered to be suitable

for information storage since the two resistance states with an abrupt switching

correspond to the distinguishable physical states.[24] Nevertheless, the sharp transition in

RS is a disadvantage for synaptic characteristics which typically need a gradual

transition. In analog RS, such gradual transition is essential.[25] Actually, coexistence of

the two RS modes have been reported in some oxides based memristors, which is

mainly dependent on the magnitude of bias voltage.[26,27] In MXene, Khot et al. reported

both analog and digital RS behaviors, but the realization depended on using different

electrodes.[28] However, the coexistence has rarely reported in MXene-based memristors

with both analog and digital RS behaviors in the same device. Furthermore, a

memristor-based hybrid analog-digital computation platform is required for mobile

robotics, in which the digital and analog modes are responsible for the high-level

algorithm, sensor fusion and motion.[29] This indicates the desirability of implementation

of the coexistence of such analog and digital RS behaviors in the same device in 2D

Ti$_3$C$_2$ nanosheets, which is expected to facilitate simplifying the manufacture complexity for complex neutral system.[29,30]

In this work, vertical memristors based on Ti$_3$C$_2$ nanosheets were fabricated with Pt as electrodes to demonstrate the coexistence of analog and digital RS behaviors in the same device. Ti$_3$C$_2$-based memristors possess excellent digital RS behaviors with a high switching ratio and good stability and reliability, suggesting the potential applications in non-volatile memory. On the other hand, analog RS behaviors can be observed under a low operation voltage. Furthermore, the basic synaptic functions can be emulated, such as long-term plasticity of long-term potentiation (LTP) and depression (LTD) as well as short-term plasticity of the paired-pulse facilitation (PPF) and depression (PPD). More importantly, the learning-forgetting experience of human brain is realized and an ANN can be constructed for image recognition.

EXPERIMENTAL SECTION

MXene Synthesis and Device Fabrication. The MXene Ti$_3$C$_2$ sample was obtained by the chemical etching of commercially purchased Ti$_3$AlC$_2$ powders (as schematically shown in Figure S1, Supporting Information). The Ti$_3$C$_2$ nanosheets were exfoliated from the etched MXene. For device fabrication, firstly, the Pt layer ($\approx$100 nm) was fabricated on a SiO$_2$ (280 nm)/Si substrate by photolithography as a bottom electrode. The exfoliated Ti$_3$C$_2$ nanosheets were transferred directly onto the top surface of the well patterned Pt bottom electrode with the assistance of polydimethylsiloxane (PDMS). Then, top Pt electrode was prepared by photolithography on the individual Ti$_3$C$_2$ nanosheets to fabricate a two-terminal vertical memristor with sandwiched structure of

Pt/Ti$_3$C$_2$/Pt, as shown in Figure S2. The detailed fabrication process can be referred to our previous work.[14]

Characterizations, Measurements and Simulations. The field emission scanning electron microscope (FESEM, JSM-7800F, Japan) was used to characterize the microstructure of the exfoliated Ti$_3$C$_2$ nanosheets. Atomic force microscope (AFM, Park Systems Crop XE7) was employed to confirm the surface morphology and thickness of the exfoliated Ti$_3$C$_2$ nanosheets. The X-ray photoelectron spectroscope (XPS, ESCALAB 250XI, Thermo Fisher, USA) was utilized to perform elemental analysis. All electrical properties were tested by using a four-probe station system equipped with a Keithley 2636B Source Meter in air at room temperature. The neural network simulations were achieved through Crosssim platform. The program code was written in Python and ran under a free integrated development environment of Spyder.

RESULTS AND DISCUSSION

The atomic structure of the Ti$_3$AlC$_2$ is schematically shown in Figure 1a. The Al atoms between Ti$_3$C$_2$ layers are etched by the chemical etching method, giving rise to the obtained layer-structure Ti$_3$C$_2$. The morphology of the Ti$_3$C$_2$ nanosheets transferred on carbon cloth is characterized by the FESEM, demonstrating the smooth surface of the exfoliated Ti$_3$C$_2$ nanosheets, as shown in Figure 1b. Then, the AFM image shows the thickness and surface morphology of the Ti$_3$C$_2$ nanosheets, as shown in Figure 1c. The thickness of the Ti$_3$C$_2$ nanosheets transferred on the SiO$_2$/Si substrate is ~ 40 nm, as shown in the inset of Figure 1c. Furthermore, XPS was used to characterize the Ti$_3$C$_2$ nanosheets transferred on a SiO$_2$/Si substrate. Figure 1d shows the XPS spectrum of Ti

2p of Ti_3C_2. The peak can be divided into four peaks located at ~454.90, 455.43, 456.30 and 458.39 eV, which are assigned to Ti−C, Ti−X, Ti_xO_y and TiO_2, respectively. The existence of TiO_2 peaks indicates that the Ti_3C_2 nanosheets is partially oxidized.[31] As we all known, natural oxidation for the 2D MXene can occur in air.[32] Thus, it is inevitable to observe the peak associated to the TiO_2. Figure 1e shows the C 1s spectrum. The peak can be divided into four peaks located at ~281.95, 284.07, 285.35 and 287.72 eV, which are assigned to C−Ti, C−C, C−H and C−O, respectively. Figure 1f shows the O 1s spectrum. The peak can be divided into three peaks located at ~530.05, 530.6, 532.5 eV, which are assigned to TiO_2, TiO_x and Ti−OH, respectively. The existence of Ti−OH peak indicates the existence of adsorbed −OH terminal groups on the surface. The peak associated with TiO_x suggests the existence of some oxygen vacancies in the partially oxidized Ti_3C_2 nanosheets.[33]

Next, the RS properties of the Ti_3C_2-based memristors are investigated. The inset in Figure 2a shows the schematic of the two-terminal device with vertical Pt/Ti_3C_2/Pt structure. Typical bipolar digital RS behaviors can be shown in Figure 2a of the current−voltage (I−V) curve with an operation voltage of 7 V in a sweeping sequence of 0 V→ 7 V→ 0 V→ − 7 V→ 0 V. It should be noted that the Pt/Ti_3C_2/Pt device is forming-free. The compliance current (I_{CC}) of 0.5 mA is set for positive scanning to prevent the generation of excessive heat caused by large current. Figure 2b shows the I−V curve with current in logarithmic scale. Initially, the device is at the high resistance state (HRS). When the voltage gradually increases to ~5.03 V, the current suddenly increases from 7.91×10^{-8} A to 5.00×10^{-4} A, resulting in the ON/OFF ratio of 6.33 ×

10^3, corresponding to the "SET" process from the HRS to the low resistance state (LRS). Then the device maintains the LRS until the voltage decreases to − 5.12 V, where a current reduction from 1.17×10^{-3} A to 1.84×10^{-8} A can be observed, corresponding to the RESET process. Moreover, multi-cycle $I−V$ curves with the bipolar RS behaviors are shown in Figure S3, demonstrating the good circle-to-circle repeatability. Figure S4 show the distributions of SET and RESET voltages, suggesting the reliability and stability of the fabricated device. In the RESET process I_{cc} is removed in order to generate sufficient Joule heat which can lead to the breakdown of the formed CFs. To further understand the RS mechanism, the positive part of the $I−V$ curve is re-plotted in double-logarithmic scale, as shown in Figure 2c. At the HRS, the curve can be divided into three regions according to the fitted slope, initially 1.17, then 2.13, and lastly 3.24. This is the typical space charge limiting current (SCLC) mechanism.[34]The dual-logarithmic $I−V$ curve in negative part also demonstrates similar fitting result, as shown in Figure S5. At the LRS, Ohmic conductive behaviors can be observed with the slope is 1.01, suggesting the formation of the conductive filaments (CFs). The oxygen vacancies play an important role in the formation of the CFs in the partially oxidized Ti_3C_2 nanosheets.[28] Under an external electric field, oxygen vacancies can migrate and accumulate to form the CFs, corresponding to the switching from HRS to LRS. Subsequently, the formed CFs can be broken under a reversed electric field, corresponding to the switching from the LRS to HRS.

Next, the retention characteristic of the $Pt/Ti_3C_2/Pt$ device is tested at room temperature at a read voltage of 0.5 V. The LRS and HRS can respectively maintain

10^4 s with an ON/OFF ratio of 5.62×10^3, as shown in Figure 2d. The endurance performance was tested at pulse mode with the pulse width (W) of 0.6 s, interval (Δt) of 2 s and amplitude (A) of 7 and -7 V, as shown in Figure 2e. The device can sustain up to 2000 cycles without overlap. Figure 2f shows the cumulative probability statistics of resistances in the LRS and HRS, which indicates that LRS and HRS are located in the range of 6.02×10^2 to 3.35×10^5 and 8.15×10^6 to 6.01×10^{10}, respectively. The HRS and LRS can be well distinguished, although there are some fluctuations in both of them. Therefore, the Pt/Ti$_3$C$_2$/Pt device exhibits typical bipolar digital RS behaviors with good stability and reliability, suggesting the potential applications in non-volatile memory.

It is intriguing that the phenomenon of coexisted digital and analog RS behaviors is observed, depending on the magnitude of operation voltage. Digital RS behaviors with two distinguished resistance states can be achieved under a high operation voltage of 7 V. While analog RS behaviors with a series of resistance states exhibiting a gradual change can be observed at a relatively low operation voltage of 4 V, as shown in Figure 3a. Under the positive voltage in a sweeping sequence of 0 V→ 4 V→ 0 V, the current at 4 V increases from 8.15×10^{-9} A to 2.06×10^{-8} A with the increase of scanning times, as shown in the inset of Figure 3a. The gradual increase trend of the current can be clearly seen in Figure 3b. Under the relatively low electric field, only some disperse CFs which do not connect the two electrodes can be formed due to the migration and accumulation of oxygen vacancies, which can slightly decrease the resistance of the Ti$_3$C$_2$ nanosheets, resulting in the observed gradual increase in current. As the scanning

times increasing, the CFs can further grow and the resistance can be accordingly reduced, giving rise to the analog RS behaviors. For negative continuous scanning, the device demonstrates a gradual decrease in the current, as shown in Figure 3c. The current decreases from -2.01×10^{-9} A to -1.18×10^{-9} A with the increase of scanning times, as presented in the inset of Figure 3c. The gradual decrease trend of the current can be clearly seen in Figure 3d. Under the reversed electric field, oxygen vacancies migrate to the opposite direction, leading to the formed CFs more disperse. Thus, the current decreases gradually as the scanning times increasing. The digital-analog coexistence also has been reported in other materials[26,35,36] (See Supporting Information, Table S1 of the comparison of the RS performance between our device with some other-materials devices that realize the digital-analog coexistence). Our fabricated memristors demonstrate comparable RS behaviors with some other devices that realize the digital-analog coexistence.

The memristive behaviors can be used to implement synaptic functions.[37,38] In the biological neural systems, the neurons are connected to each other by synapses. The synapse is composed of presynaptic terminal, synaptic cleft, and postsynaptic terminal,[39,40] as schematically shown in Figure 4a. The secretion of neurotransmitters can transmit biological signals from one neuron to another, and the self-transmitted signals can regulate the strength of synaptic connections, which is called synaptic plasticity.[41,42] The synaptic plasticity can be indicated by the change of current in the Ti_3C_2-based two-terminal memristors which can serve as an artificial synapse. PPF and PPD are the two types of short-term plasticity which can also be implemented based on

the memristors. The PPD index can be calculated by equation of $(A_2 - A_1)/A_1 \times 100\%$, where A_1 and A_2 are the synaptic current stimulated by two consecutive <u>negative voltage pulses</u> with different pulse intervals.[43] Typically, the A_2 is less than A_1 due to the depression effects of negative voltages. <u>Figure 4b shows the PPD index as a function of Δt when stimulated by the two consecutive negative voltage pulses (A = − 4 V, W = 0.2 s),</u> indicating that the PPD index decays with increasing Δt. In addition, the PPF index can be calculated by the same equation, where the A_2 is typically larger than A_1 due to the potentiation effects of positive voltages. <u>The PPF index decays with increasing Δt when stimulated by the two consecutive positive voltage pulses (A = 4 V, W = 0.2 s),</u> as shown in Figure 4c.The decay characteristics of PPD and PPF index remain consistent with the biological synaptic behaviors.[44] Furthermore, long-term plasticity of LTP and LTD can be implemented based on the memristors. Figures S3a−c show the LTP behaviors under stimulations of positive pulse sequences. The increased pulse amplitude, wider pulse width or shorter pulse interval can produce relatively strengthened potentiation effects. Figures S6d−f show the LTD behaviors under stimulations of negative pulse sequences. Similarly, the increased pulse amplitude, wider pulse width or shorter pulse interval can produce relatively strengthened depression effects. By optimizing the pulse parameters, we can achieve the more linear LTP and LTD functions, as shown in Figure 4d. When $W = 0.2$ s, $\Delta t = 0.3$ s and $A = 4$ V, with the increase of pulse numbers, the current increases from 4069 nA to 7905 nA, corresponding to the LTP. When $W = 0.2$ s, $\Delta t = 0.3$ s and $A = − 4$ V, the current is reduced to 4073 nA, corresponding to the LTD. Then, continuous LTP/LTD functions

have been studied, as shown in Figure 4e. 11 sets of consecutive LTP/LTD cycles with good repeatability are demonstrated, indicating the LTP/LTD functions can be repeatedly implemented.

The "learning-forgetting" experience of human brain is simulated by the Ti_3C_2-based artificial synapses, as shown in Figure 5a. The current is gradually increased to 334 nA during the stimulation of 20 voltage pulses (W = 50 ms, Δt = 200 ms and A = 4 V), corresponding to the learning process. Then the current gradually decreases to 238 nA during the period in the absence of pulse stimulation, corresponding to the forgetting process. In contrast to the stimulation of 20 pulses in the learning process, only 13 pulses are needed to increase to the same current level for the subsequent relearning process. This is very similar to learning experience of people who can spend less study to reach to the same cognitive level in the relearning process. Figure 5b shows four "learning-forgetting" cycles. Although the current decays in the forgetting process, the current increases compared with the initial value after every "learning-forgetting" period. Take the first learning process as example, the current is increased by ΔI_1 after the learning process, implying people can improve their cognitive level through learning experience. And the increased current (ΔI) continues to grow in amplitude ($\Delta I_4 > \Delta I_3 > \Delta I_2 > \Delta I_1$) by continuous learning process, suggesting the impact of relearning.

To estimate the computing performance of the artificial synapse, the ANN with three layers of the input, hidden and output layers can be established based on CrossSim platform, as shown in Figure 6a. In the simulation, N × M devices are modelled in an N × M crossbar array. Figure 6b shows the input and output terminal, which are defined

12

as the neurons in the input and output layers respectively. In the simulation, the small image with 8×8 pixels and large image with 28×28 pixels are employed for the training and test. <u>20 sets of repeatable LTP/LTD circles (Figure S7, Supporting Information) measured experimentally are used for image recognition.</u> Figure 6c shows the recognition accuracy as a function of the iteration number for small image. The recognition accuracy reaches up to 79.8% after 40 training epochs. Figure 6d shows that the recognition accuracy can be maintained at 80.6% for large image. The recognition accuracy is lower than the that under ideal software conditions (97%), However, we will improve the recognition accuracy by modulating the device structure and optimizing synaptic functions in future. This simulation still can prove that our Ti$_3$C$_2$-based memristors have the potential to be used as an artificial synapse for future neuromorphic computing.

CONCLUSIONS

In summary, we have fabricated a Ti$_3$C$_2$-based memristors that implement digital and analog RS behaviors in the same device. The RS behaviors and the synaptic functions of Ti$_3$C$_2$-based memristors under electrical stimuli are systematically investigated. Under a high operation voltage, the memristors demonstrate typical bipolar RS behaviors with a high ON/OFF ratio, good endurance and retention characteristics, suggesting potential applications in non-volatile memory. On the other hand, analog RS behaviors can be achieved under a relatively low operation voltage. The basic synaptic functions including LTP, LTD, STP, PPF and PPD are realized based on the memristors. In addition, "learning-forgetting" experience can be emulated under stimulations of

pulse voltages. More importantly, the artificial synapses can construct an ANN to implement image recognition with high accuracy. All these studies show coexistence of digital and analog RS behaviors in 2D Ti_3C_2 nanosheets, suggesting the potential applications in non-volatile memory and neuromorphic computing.

ASSOCIATED CONTENT

Supporting Information

The Supporting information is available free of charge on the ACS Publications website at DOI:

The schematic of the etching process of the MXene Ti_3C_2, the optical image of the device, multi-cycle $I-V$ curves of the memristor, distributions of the SET and REST voltages, dual-logarithmic fitting of the negative part of the $I-V$ curve, synaptic behaviors of LTP and LTD, 20 sets of LTP/LTD cycles and the table of the comparison of the RS performance, comparison of the RS performance between our device with some other-similar-materials devices that realize the digital-analog coexistence.

AUTHOR INFORMATION

Corresponding Author

Wenjing Jie: College of Chemistry and Materials Science, Sichuan Normal University, Chengdu, 610066, China. Email: wenjing.jie@sicnu.edu.cn

Jianhua Hao: Department of Applied Physics, The Hong Kong Polytechnic University, Hung Hom, Kowloon, Hong Kong, China. Email: jh.hao@polyu.edu.hk

Notes

REFERENCES

(1)   Sun, B.; Guo, T.; Zhou, G.; Ranjan, S.; Jiao, Y.; Wei, L.; Zhou, Y. N.; Wu, Y. A. Synaptic Devices Based Neuromorphic Computing Applications in Artificial Intelligence. *Mater. Today Phys.* **2021**, *18*, 100393.

(2)   Li, J.; Dwivedi, P.; Kumar, K. S.; Roy, T.; Crawford, K. E.; Thomas, J. Growing Perovskite Quantum Dots on Carbon Nanotubes for Neuromorphic Optoelectronic Computing. *Adv. Electron. Mater.* **2021**, *7* (1), 2000535.

(3)   Upadhyay, N. K.; Jiang, H.; Wang, Z.; Asapu, S.; Xia, Q.; Joshua Yang, J. Emerging Memory Devices for Neuromorphic Computing. *Adv. Mater. Technol.* **2019**, *4* (4), 1800589.

(4)   Ma, F.; Zhu, Y.; Xu, Z.; Liu, Y.; Zheng, X.; Ju, S.; Li, Q.; Ni, Z.; Hu, H.; Chai, Y.; Wu, C.; Kim, T. W.; Li, F. Optoelectronic Perovskite Synapses for Neuromorphic Computing. *Adv. Funct. Mater.* **2020**, *30* (11), 1908901.

(5)   Liao, K.; Lei, P.; Tu, M.; Luo, S.; Jiang, T.; Jie, W.; Hao, J. Memristor Based on Inorganic and Organic Two-Dimensional Materials: Mechanisms, Performance, and Synaptic Applications. *ACS Appl. Mater. Interfaces* **2021**, *13* (28), 32606–32623.

(6)   Cao, Q.; Lü, W.; Wang, X. R.; Guan, X.; Wang, L.; Yan, S.; Wu, T.; Wang, X. Nonvolatile Multistates Memories for High-Density Data Storage. *ACS Appl. Mater. Interfaces* **2020**, *12* (38), 42449–42471.

(7)   Peng, Z.; Wu, F.; Jiang, L.; Cao, G.; Jiang, B.; Cheng, G.; Ke, S.; Chang, K. C.; Li, L.; Ye, C. HfO$_2$-Based Memristor as an Artificial Synapse for Neuromorphic Computing with Tri-Layer HfO$_2$/BiFeO$_3$/HfO$_2$ Design. *Adv. Funct. Mater.* **2021**, *31* (48), 2107131.

(8)   Yuan, J.; Lou, J. 2D Materials: Memristor Goes Two-Dimensional. *Nat. Nanotechnol.* **2015**, *10* (5), 389–390.

(9)   Yeon, C.; Yun, S. J.; Yang, J.; Youn, D. H.; Lim, J. W. Na-Cation-Assisted Exfoliation of MX$_2$ (M = Mo, W; X = S, Se) Nanosheets in an Aqueous Medium with the Aid of a Polymeric Surfactant for Flexible Polymer-Nanocomposite Memory Applications. *Small* **2018**, *14* (2), 1702747.

(10)   Meng, J. L.; Wang, T. Y.; He, Z. Y.; Chen, L.; Zhu, H.; Ji, L.; Sun, Q. Q.; Ding,

S. J.; Bao, W. Z.; Zhou, P.; Zhang, D. W. Flexible Boron Nitride-Based Memristor for: In Situ Digital and Analogue Neuromorphic Computing Applications. *Mater. Horizons* **2021**, *8* (2), 538–546.

(11) Huh, W.; Lee, D.; Lee, C. H. Memristors Based on 2D Materials as an Artificial Synapse for Neuromorphic Electronics. *Adv. Mater.* **2020**, *32* (51), 2002092.

(12) Duan, H.; Cheng, S.; Qin, L.; Zhang, X.; Xie, B.; Zhang, Y.; Jie, W. Low-Power Memristor Based on Two-Dimensional Materials. **2022**, *13*, 7130–7138.

(13) Guo, F.; Song, M.; Wong, M. C.; Ding, R.; Io, W. F.; Pang, S. Y.; Jie, W.; Hao, J. Multifunctional Optoelectronic Synapse Based on Ferroelectric Van Der Waals Heterostructure for Emulating the Entire Human Visual System. *Adv. Funct. Mater.* **2022**, *32* (6), 2108014.

(14) Lei, P.; Duan, H.; Qin, L.; Wei, X.; Tao, R.; Wang, Z.; Guo, F.; Song, M.; Jie, W.; Hao, J. High-Performance Memristor Based on 2D Layered BiOI Nanosheet for Low-Power Artificial Optoelectronic Synapses. *Adv. Funct. Mater.* **2022**, *32*(25), 2201276.

(15) Zhang, C. (John); McKeon, L.; Kremer, M. P.; Park, S. H.; Ronan, O.; Seral-Ascaso, A.; Barwich, S.; Coileáin, C.; McEvoy, N.; Nerl, H. C.; Anasori, B.; Coleman, J. N.; Gogotsi, Y.; Nicolosi, V. Additive-Free MXene Inks and Direct Printing of Micro-Supercapacitors. *Nat. Commun.* **2019**, *10* (1), 1795.

(16) Wu, Y.; Sun, Y.; Zheng, J.; Rong, J.; Li, H.; Niu, L. MXenes: Advanced Materials in Potassium Ion Batteries. *Chem. Eng. J.* **2021**, *404*, 126565.

(17) Pang, S. Y.; Wong, Y. T.; Yuan, S.; Liu, Y.; Tsang, M. K.; Yang, Z.; Huang, H.; Wong, W. T.; Hao, J. Universal Strategy for HF-Free Facile and Rapid Synthesis of Two-Dimensional MXenes as Multifunctional Energy Materials. *J. Am. Chem. Soc.* **2019**, *141* (24), 9610–9616.

(18) Pang, S. Y.; Io, W. F.; Hao, J. Facile Atomic-Level Tuning of Reactive Metal–Support Interactions in the Pt QDs@ HF-Free MXene Heterostructure for Accelerating PH-Universal Hydrogen Evolution Reaction. *Adv. Sci.* **2021**, *8* (22), 2102207.

(19) Song, M.; Pang, S. Y.; Guo, F.; Wong, M. C.; Hao, J. Fluoride-Free 2D Niobium Carbide MXenes as Stable And Biocompatible Nanoplatforms for Electrochemical Biosensors with Ultrahigh Sensitivity. *Adv. Sci.* **2020**, *7* (24), 2001546.

(20) Wang, Y.; Gong, Y.; Yang, L.; Xiong, Z.; Lv, Z.; Xing, X.; Zhou, Y.; Zhang, B.; Su, C.; Liao, Q.; Han, S. T. MXene-ZnO Memristor for Multimodal In-Sensor Computing. *Adv. Funct. Mater.* **2021**, *31* (21), 2100144.

(21) Melianas, A.; Kang, M. A.; VahidMohammadi, A.; Quill, T. J.; Tian, W.; Gogotsi, Y.; Salleo, A.; Hamedi, M. M. High-Speed Ionic Synaptic Memory Based on 2D Titanium Carbide MXene. *Adv. Funct. Mater.* **2022**, *32* (12), 2109970.

(22) Chen, Y.; Wang, Y.; Luo, Y.; Liu, X.; Wang, Y.; Gao, F.; Xu, J.; Hu, E.; Samanta, S.; Wan, X.; Lian, X.; Xiao, J.; Tong, Y. Realization of Artificial Neuron Using MXene Bi-Directional Threshold Switching Memristors. *IEEE Electr. Device L.* **2019**, *40* (10), 1686–1689.

(23)   Guo, L.; Mu, B.; Li, M. Z.; Yang, B.; Chen, R. S.; Ding, G.; Zhou, K.; Liu, Y.; Kuo, C. C.; Han, S. T.; Zhou, Y. Stacked Two-Dimensional MXene Composites for an Energy-Efficient Memory and Digital Comparator. *ACS Appl. Mater. Interfaces* **2021**, *13* (33), 39595–39605.

(24)   Zidan, M. A.; Strachan, J. P.; Lu, W. D. The Future of Electronics Based on Memristive Systems. *Nat. Electron.* **2018**, *1* (1), 22–29.

(25)   Mao, S.; Sun, B.; Zhou, G.; Yang, Y.; Zhao, H.; Zhou, Y.; Chen, Y.; Zhao, Y. Analog-to-Digital and Self-Rectifying Resistive Switching Behavior Based on Flower-like δ-MnO_2. *Appl. Surf. Sci.* **2022**, *595*, 153560.

(26)   Li, Y.; Chu, J.; Duan, W.; Cai, G.; Fan, X.; Wang, X.; Wang, G.; Pei, Y. Analog and Digital Bipolar Resistive Switching in Solution-Combustion-Processed NiO Memristor. *ACS Appl. Mater. Interfaces* **2018**, *10* (29), 24598–24606.

(27)   He, Z. Y.; Wang, T. Y.; Meng, J. L.; Zhu, H.; Ji, L.; Sun, Q. Q.; Chen, L.; Zhang, D. W. CMOS Back-End Compatible Memristors for: In Situ Digital and Neuromorphic Computing Applications. *Mater. Horizons* **2021**, *8* (12), 3345–3355.

(28)   Khot, A. C.; Dongale, T. D.; Park, J. H., Kesavan, A. V.; Kim, T. G. Ti_3C_2-Based MXene Oxide Nanosheets for Resistive Memory and Synaptic Learning Applications. *ACS Appl. Mater. Interfaces* **2021**, *13*, 5216−5227.

(29)   Kassanos, P. Analog-Digital Computing Let Robots Go through the Motions. *Sci. Robot.* **2020**, *5* (47), eabe6818.

(30)   Liu, B.; Hu, M.; Li, H.; Mao, Z. H.; Chen, Y. R.; Huang, T. W.; Zhang, W. Digital-assisted noise-eliminating training for memristor crossbar-based analog neuromorphic computing engine," in Proc. 50th ACM EDAC IEEE Design Autom. Conf. (DAC), 2013, pp. 1−6.

(31)   Kim, S. J.; Koh, H. J.; Ren, C. E.; Kwon, O.; Maleski, K.; Cho, S. Y.; Anasori, B.; Kim, C. K.; Choi, Y. K.; Kim, J.; Gogotsi, Y.; Jung, H. T. Metallic $Ti_3C_2T_x$ MXene Gas Sensors with Ultrahigh Signal-to-Noise Ratio. *ACS Nano* **2018**, *12* (2), 986−993.

(32)   Halim, J.; Lukatskaya, M. R.; Cook, K. M.; Lu, J.; Smith, C. R.; Näslund, L. Å.; May, S. J.; Hultman, L.; Gogotsi, Y.; Eklund, P.; Barsoum, M. W. Transparent Conductive Two-Dimensional Titanium Carbide Epitaxial Thin Films. *Chem. Mater.* **2014**, *26* (7), 2374−2381.

(33)   Khot, A. C.; Dongale, T. D.; Park, J. H.; Kesavan, A. V.; Kim, T. G. Ti_3C_2-Based MXene Oxide Nanosheets for Resistive Memory and Synaptic Learning Applications. *ACS Appl. Mater. Interfaces* **2021**, *13* (4), 5216−5227.

(34)   Bai, N.; Xu, M.; Hu, C.; Ma, Y.; Wang, Q.; He, D.; Qi, J.; Li, Y. Resistive Switching Behaviors Mediated by Grain Boundaries in One Longitudinal Al/MoS_2&PVP/ITO Device. *Mat. Sci. Semicon. Proc.* **2019**, *91*, 246−251.

(35)   Lin, Y.; Wang, C.; Ren, Y.; Wang, Z.; Xu, H.; Zhao, X.; Ma, J.; Liu, Y. Analog−Digital Hybrid Memristive Devices for Image Pattern Recognition with Tunable Learning Accuracy and Speed. *Small Methods* **2019**, *3* (10), 1900160.

(36)   Zhang, Y.; Wang, L.; Chen, H.; Ma, T.; Lu, X.; Loh, K. P. Analog and Digital Mode α-In_2Se_3 Memristive Devices for Neuromorphic and Memory

Applications. *Adv. Electron. Mater.* **2021**, *7* (12), 2100609.

(37) Wang, Z.; Wang, L.; Wu, Y.; Bian, L.; Nagai, M.; Jv, R.; Xie, L.; Ling, H.; Li, Q.; Bian, H.; Yi, M.; Shi, N.; Liu, X.; Huang, W. Signal Filtering Enabled by Spike Voltage-Dependent Plasticity in Metalloporphyrin-Based Memristors. *Adv. Mater.* **2021**, *33* (43), 2104370.

(38) Bian, H.; Goh, Y. Y.; Liu, Y.; Ling, H.; Xie, L.; Liu, X. Stimuli-Responsive Memristive Materials for Artificial Synapses and Neuromorphic Computing. *Adv. Mater.* **2021**, *33* (46), 2006469.

(39) Biederer, T.; Kaeser, P. S.; Blanpied, T. A. Transcellular Nanoalignment of Synaptic Function. *Neuron* **2017**, *96* (3), 680−696.

(40) Hussain, T.; Abbas, H.; Youn, C.; Lee, H.; Boynazarov, T.; Ku, B.; Jeon, Y. R.; Han, H.; Lee, J. H.; Choi, C.; Choi, T. Cellulose Nanocrystal Based Bio-Memristor as a Green Artificial Synaptic Device for Neuromorphic Computing Applications. *Adv. Mater. Technol.* **2022**, *7* (2), 2100744.

(41) Jo, S. H.; Chang, T.; Ebong, I.; Bhadviya, B. B.; Mazumder, P.; Lu, W. Nanoscale Memristor Device as Synapse in Neuromorphic Systems. *Nano Lett.* **2010**, *10* (4), 1297−1301.

(42) Van De Burgt, Y.; Melianas, A.; Keene, S. T.; Malliaras, G.; Salleo, A. Organic Electronics for Neuromorphic Computing. *Nat. Electron.* **2018**, *1* (7), 386−397.

(43) Luo, S.; Liao, K.; Lei, P.; Jiang, T.; Chen, S.; Xie, Q.; Luo, W.; Huang, W.; Yuan, S.; Jie, W.; Hao, J. A Synaptic Memristor Based on Two-Dimensional Layered WSe_2 Nanosheets with Short- and Long-Term Plasticity. **2021**, *13* (13), 6654−6660.

(44) Wang, W.; Gao, S.; Li, Y.; Yue, W.; Kan, H.; Zhang, C.; Lou, Z.; Wang, L.; Shen, G. Artificial Optoelectronic Synapses Based on $TiN_xO_{2−x}/MoS_2$ Heterojunction for Neuromorphic Computing and Visual System. *Adv. Funct. Mater.* **2021**, *31* (34), 2101201.
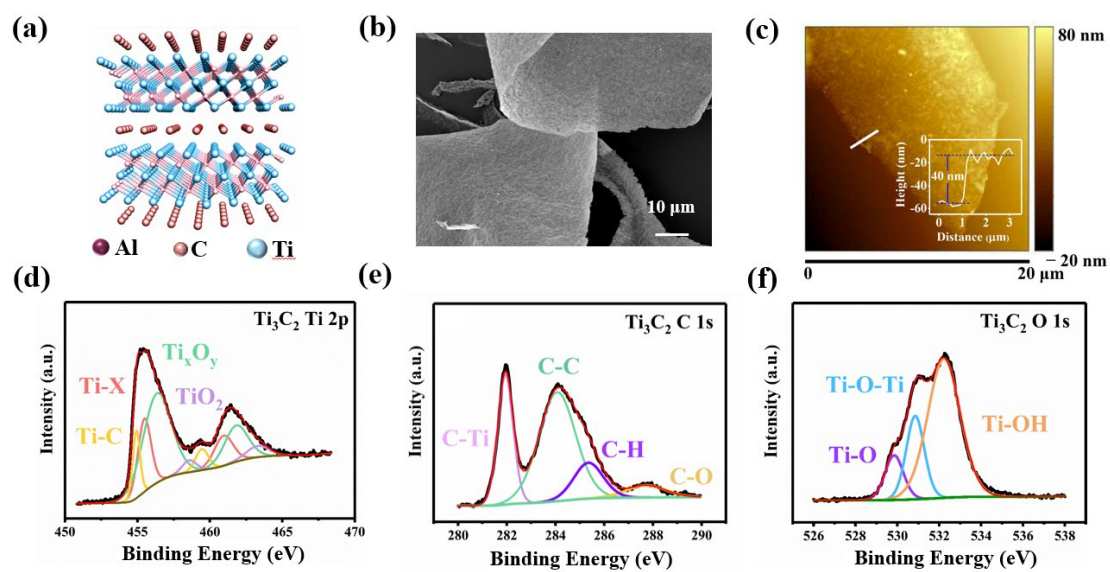
Figure 1. Characterizations of 2D Ti_3C_2 nanosheets. (a) Schematic of the atomic structure of Ti_3AlC_2. (b) FESEM image of Ti_3C_2 nanosheets. (c) AFM image of Ti_3C_2 nanosheets. The inset shows the height profile corresponding to the white line in the AFM image. XPS spectrum of Ti_3C_2 nanosheets of (d) Ti, (e) C, and (f) O elements.
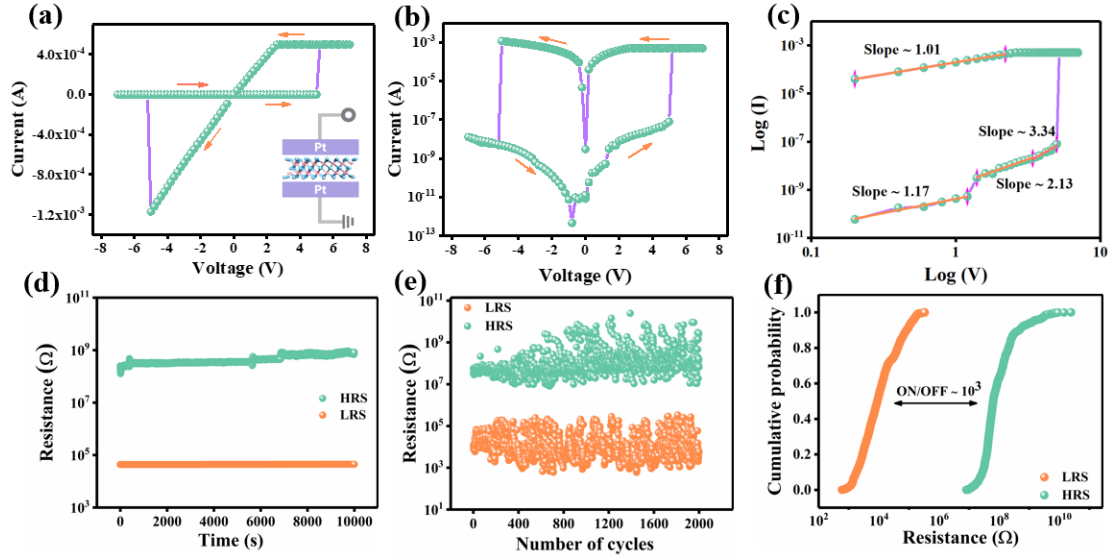
Figure 2. Digital RS behaviors of the Ti_3C_2 nanosheet. (a) Typical $I{-}V$ curve of Pt/Ti_3C_2/Pt device in linear scale. Inset shows the schematic of device structure. (b) Typical $I{-}V$ curve of Pt/Ti_3C_2/Pt device with current in logarithmic scale. (c) Positive part of the $I{-}V$ curve in double logarithmic scale. (d) Retention characteristics. (e) Endurance performance. (f) Cumulative probability diagram of the HRS and LRS.
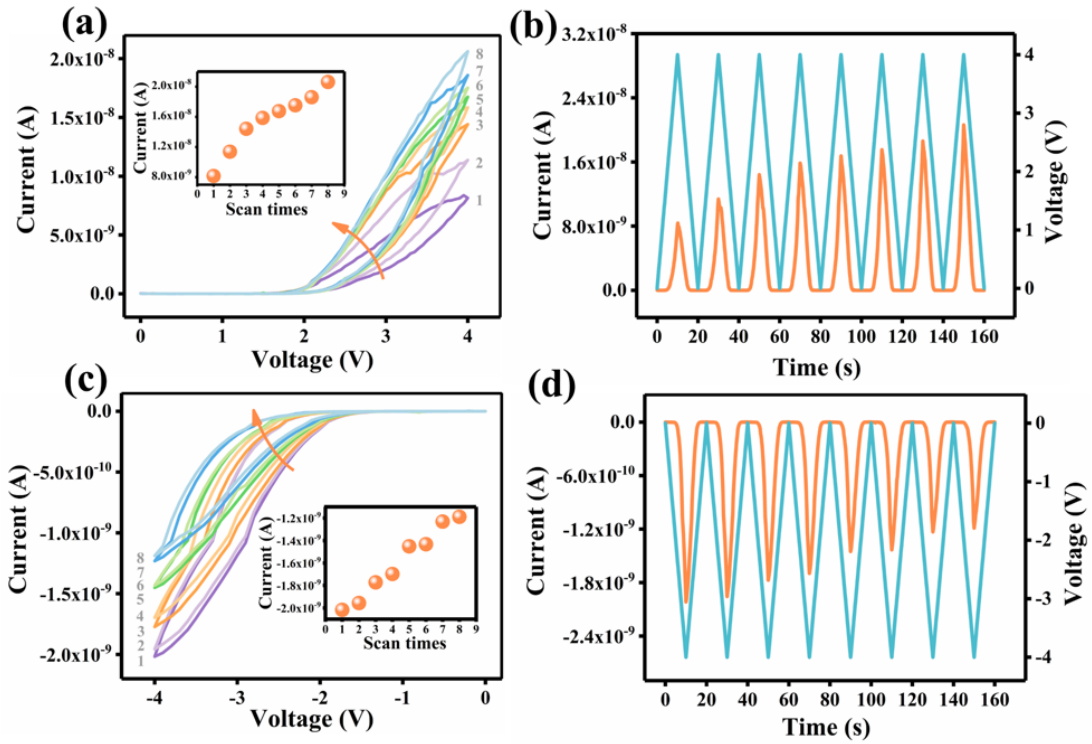
Figure 3. Analog RS behaviors of the Ti_3C_2 nanosheet. (a) $I-V$ curves of 8 consecutive cycles under positive voltage (0 V→ + 4 V→ 0 V). Inset shows the detailed current change at 4V as a function of the scan times. (b) Current and voltage data in the 8 consecutive cycles as a function of time under positive voltages. (c) $I-V$ curves of 8 consecutive cycles under negative voltage (0 V→ − 4 V→ 0 V). Inset shows the detailed current change at − 4V as a function of the scan times. (d) Current and voltage data in the 8 consecutive cycles as a function of time under negative voltages.
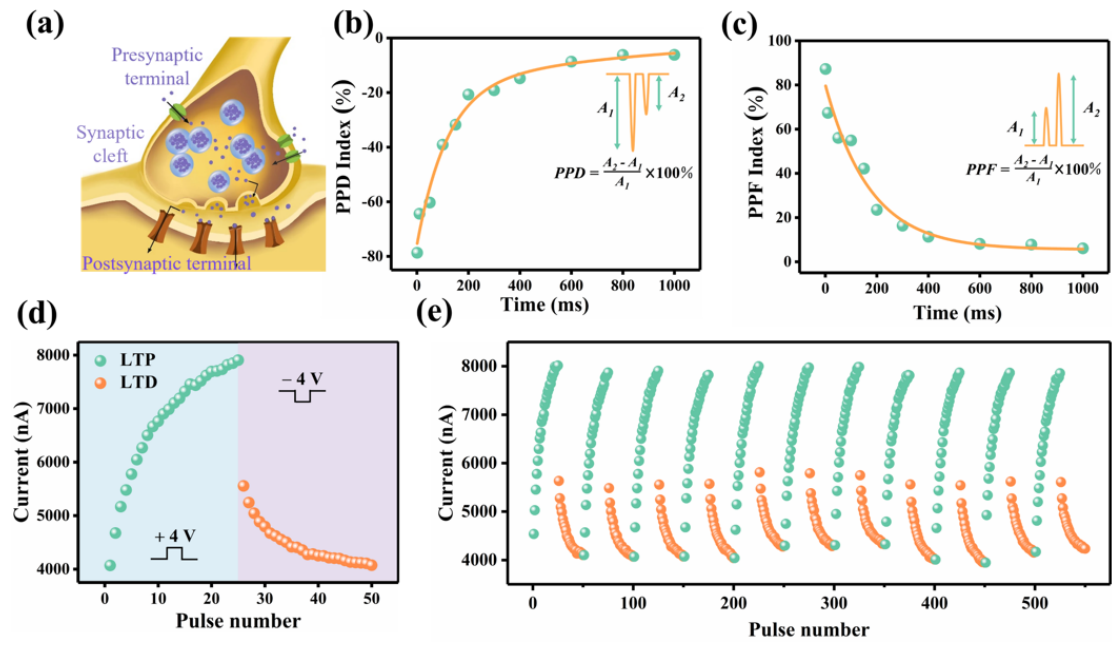
Figure 4. Synaptic behaviors of the Ti_3C_2 nanosheet. (a) Schematic of an artificial synapse. (b) The variation of PPD index as a function of the interval of the negative pulse pairs. (c) The variation of PPF index as a function of the interval of the positive pulse pairs. (d) LTP and LTD functions (e) The repeatable 11 sets of LTP/LTD circles.
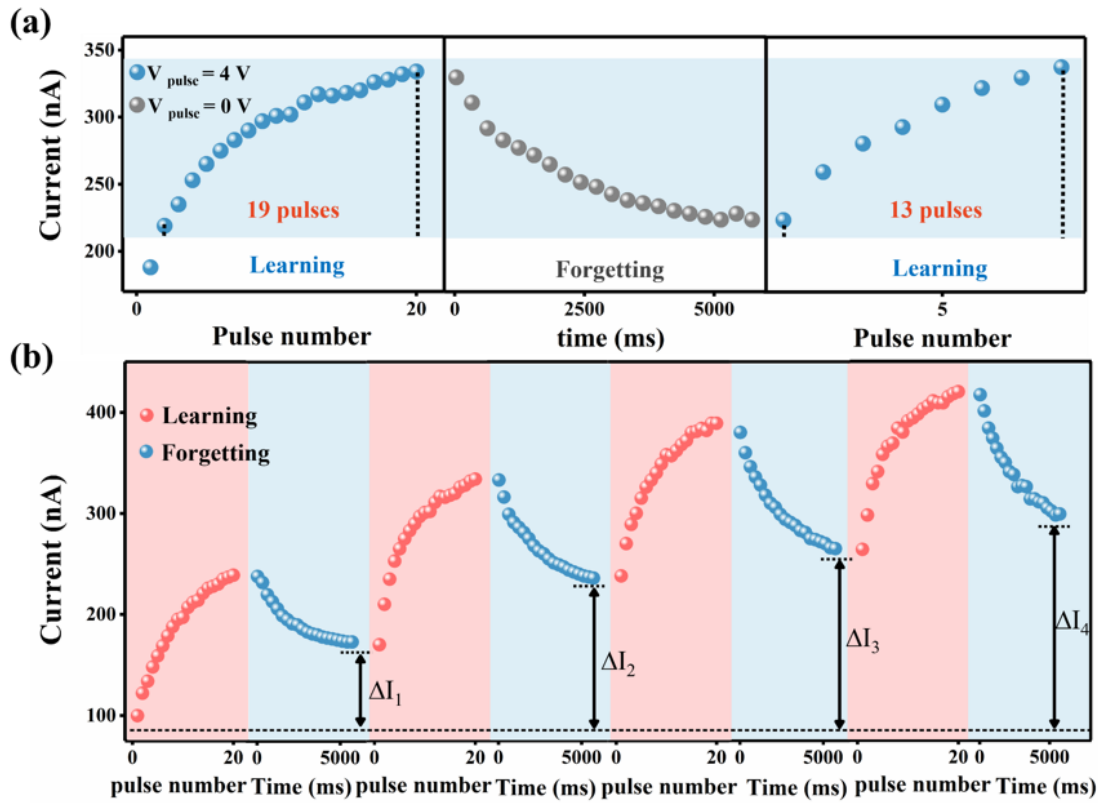
Figure 5. The "learning-forgetting" experience. (a) The learning-forgetting-relearning process. (b) The four continuous cycles of learning-forgetting process.
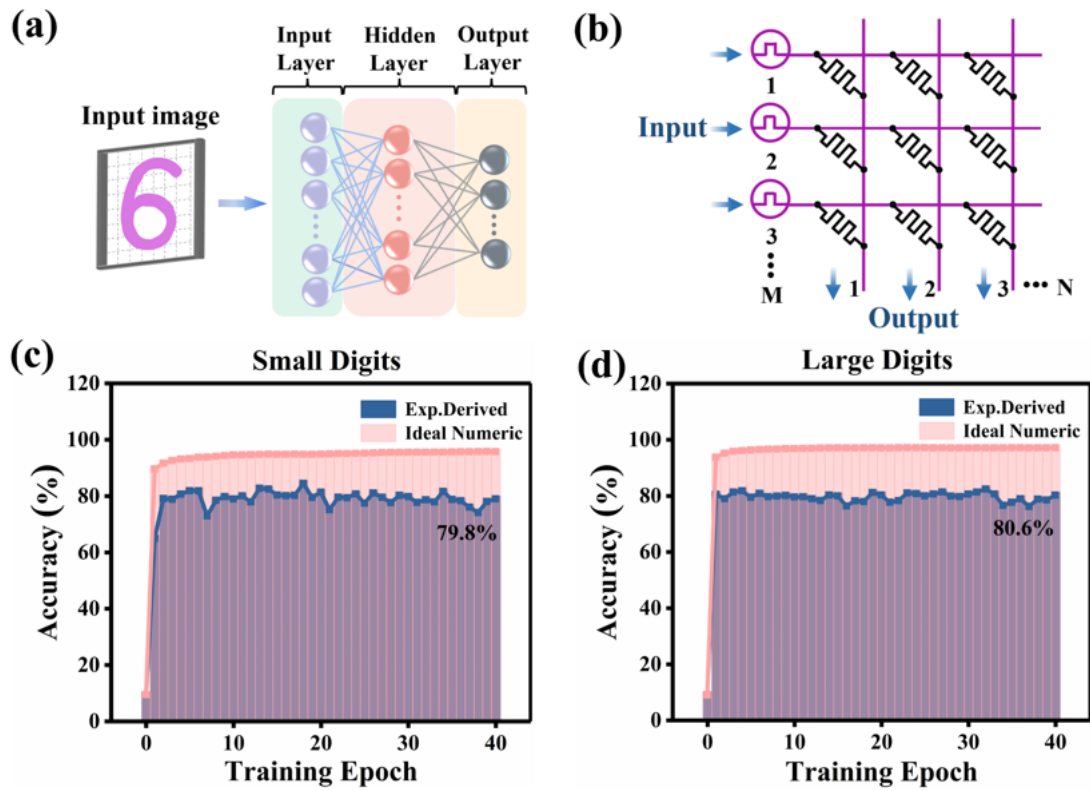
Figure 6. The ANN based on the Ti_3C_2 nanosheet for image recognition. (a) Schematic of a three-layer ANN. (b) Schematic of crossbar array for matrix operations. (c) Recognition accuracy of ANN for small image with 8×8 pixels. (d) Recognition accuracy of ANN for large image with 28×28 pixels.

TOC